

Fermilab



Nano-compositional imaging of the lanthanum silicide system at THz wavelength

FERMILAB-PUB-24-0905-SQMS-V

This manuscript has been authored by Fermi Research Alliance, LLC
under Contract No. DE-AC02-07CH11359 with the U.S. Department of Energy,
Office of Science, Office of High Energy Physics.



Nano-compositional imaging of the lanthanum silicide system at THz wavelengths

R. H. J. KIM,¹  A. K. PATHAK,^{2,3} J.-M. PARK,¹ M. IMRAN,¹
S. J. HAEUSER,¹ Z. FEI,¹ Y. MUDRYK,¹ T. KOSCHNY,¹
AND J. WANG^{1,*} 

¹Department of Physics & Astronomy, Iowa State University and Ames National Laboratory, US
Department of Energy, Ames, Iowa 50011, USA

²Department of Physics, SUNY Buffalo State University, Buffalo, NY 14222, USA

³Present address: GE Research 1 Research Cir, Niskayuna, NY 12309, USA

*jwang@ameslab.gov

Abstract: Terahertz scattering-type scanning near-field optical microscopy (THz-sSNOM) provides a noninvasive way to probe the low frequency conductivity of materials and to characterize material compositions at the nanoscale. However, the potential capability of atomic compositional analysis with THz nanoscopy remains largely unexplored. Here, we perform THz near-field imaging and spectroscopy on a model rare-earth alloy of lanthanum silicide (La–Si) which is known to exhibit diverse compositional and structural phases. We identify subwavelength spatial variations in conductivity that is manifested as alloy microstructures down to much less than 1 μm in size and is remarkably distinct from the surface topography of the material. Signal contrasts from the near-field scattering responses enable mapping the local silicon/lanthanum content differences. These observations demonstrate that THz-sSNOM offers a new avenue to investigate the compositional heterogeneity of material phases and their related nanoscale electrical as well as optical properties.

© 2024 Optica Publishing Group under the terms of the [Optica Open Access Publishing Agreement](#)

1. Introduction

Latest advances in scattering-type scanning near-field optical microscopy (sSNOM) techniques have had an exceptional impact on nanoscale-resolved optical imaging [1–8]. Near-field measurements with sSNOM can effectively map the local information of the material properties with nanometer spatial precision. As light shines on a sharp metal tip, optical electric fields concentrate at the end of the tip and induce polarization charges in dielectrics or currents and spatial redistribution of free charge carriers in metals at the surface beneath it to follow the oscillations of the illuminating light field. The sSNOM tip with its radius of curvature that is orders of magnitude smaller than the operating wavelength establish novel ways to control and probe near-field electrodynamic responses in various systems. sSNOM has recently been extended to light frequencies down to the terahertz (THz) spectral region. Taking advantage of broadband THz pulses, THz-sSNOM has offered insights to real-space and time-domain characterizations of local variations in this low-energy range [9–19].

Nanospectroscopy performed at infrared frequencies have shown the possibility for near-field chemical identification and sensitive compositional mapping based on by probing the molecular vibrational absorption spectra or phonon responses [20,21]. On the other hand, the low-frequency THz region that extends beyond the far-infrared is ideal for accessing the fundamental low-frequency resonances and dissipationless conductivity peaks associated with collective-mode electrodynamic in quantum materials [22–26]. To this end, by enhancing conventional THz and ultrafast spectroscopy on the study of topological, magnetic and correlated materials [27–32] with the integration of a near-field measurement strategy at the nanoscale, sSNOM can be further expanded to probe local electrodynamic and/or compositional fingerprints.

2. Terahertz nano-imaging and nano-spectroscopy of rare-earth alloy

Here, we use time-domain THz scattering-type scanning near-field optical microscopy (THz-sSNOM) [18,19] to examine the contrasts in the near-field Drude response from a lanthanum–silicon (La–Si) system [33]. This sample of $\text{La}_{20}\text{Si}_{80}$ stoichiometry serves as a model system for extracting the local variations in its alloy composition due to its contrasting microstructures that are either metallic LaSi_2 or insulating silicon ($\text{LaSi}_2 + \langle \text{Si} \rangle$). Our compact sSNOM setup is home-built and based on a tapping-mode atomic force microscope with a metallic tip as depicted in Fig. 1(a). The tip acts as an antenna that receives and transmits far-field THz radiation and amplifies the near-field interaction through resonant and geometric enhancement of the THz field. Ultrafast THz pulses are generated by optical rectification in an organic THz emitter OH1 driven by a Yb fiber laser operating at a repetition rate of 1 MHz with a pulse width of 150 fs and a center wavelength at 1038 nm. THz electric fields are detected via electro-optic sampling in a CdTe crystal, and near-field signals s_n are then extracted by demodulating the backscattered radiation collected from the tip-sample system at n th harmonics of the tip-tapping frequency ($n = 1, 2$). To obtain near-field images, the tip was raster scanned over the sample, recording the s_2 signal as a function of tip position, while the THz sampling delay was fixed to a position that gives the maximum amplitude of the THz signal, as shown by the dashed line at ~ 3 ps in Fig. 1(b). The second harmonic signal s_2 from tip-sample modulation mainly consists of a dominant scattered near-field interacting with the polarizable surface of the sample [18]. Nanospectroscopy is achieved by scanning the THz sampling delay to directly trace out the oscillating THz electric field waveform in the time domain while the tip sits at a fixed location on the sample.

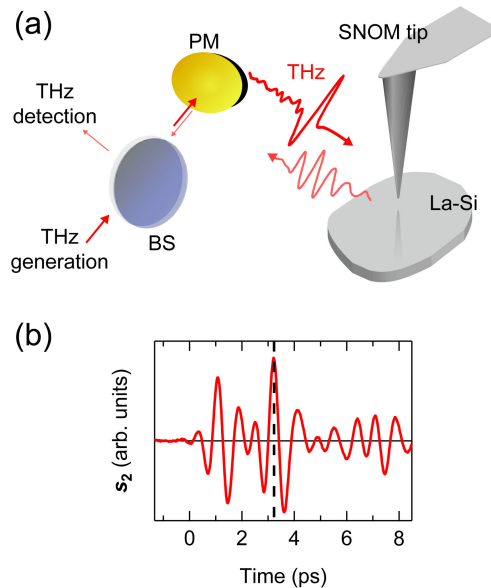


Fig. 1. (a) Schematic of the experimental setup showing the incident and scattered THz pulse from an AFM tip above the La–Si alloy. PM: parabolic mirror. BS: silicon beam splitter. (b) A typical time-resolved THz near-field waveform measured from La–Si.

Polycrystalline $\text{La}_{20}\text{Si}_{80}$ alloy was prepared by arc-melting of constituent elements: La (99.95 wt.% pure with respect to all other elements in the periodic table, provided by the Materials Preparation Center of Ames National Laboratory, USA) and Si (99.9995 wt.% pure, provided by Alfa Aesar) in a Zr-gettered Ar atmosphere on a water-cooled copper hearth using tungsten

electrode. The alloy was re-melted six times, flipping the button upside down after each melting to promote chemical homogeneity. The weight losses during melting were less than 1%.

The phase analysis of the sample was performed at room temperature using a laboratory Rigaku TTRAX powder diffractometer equipped with Mo $K\alpha$ radiation. The data were collected from 6 to 52 degree 2θ range, with a 0.01° step of 2θ measuring each data point for 2 seconds as shown in Fig. 2. Rietveld refinement of the powder X-ray diffraction data was carried out using FullProf [34]. The analysis unambiguously identified LaSi_2 phase adopting the $\alpha\text{-ThSi}_2$ crystal structure prototype, as well as pure Si, to be present in the prepared alloy, in accordance with the phase diagram of La–Si [33]. The weight ratio of the phases was 79 wt.% of LaSi_2 to 21 wt.% of Si (or 35 to 65 mol.%, respectively), in full agreement with the expected ratio of these phases according to the stoichiometry. The lattice parameters of LaSi_2 (space group $I4_1/amd$) are $a = 4.3220 \pm 2 \text{ \AA}$, $c = 13.8544 \pm 7 \text{ \AA}$, and the lattice parameter of Si is $a = 5.4306 \pm 5 \text{ \AA}$. We note that the lattice parameters of LaSi_2 are well within the range of values provided by Ref. [33], while the lattice parameter of Si agrees with literature within three experimental deviations. The profile reliability factors of the refinement are $R_p = 4.6\%$, $R_{wp} = 6.1\%$, and Bragg residuals for the individual phases were $R_B = 3.5\%$ for LaSi_2 and $R_B = 4.4$ for Si.

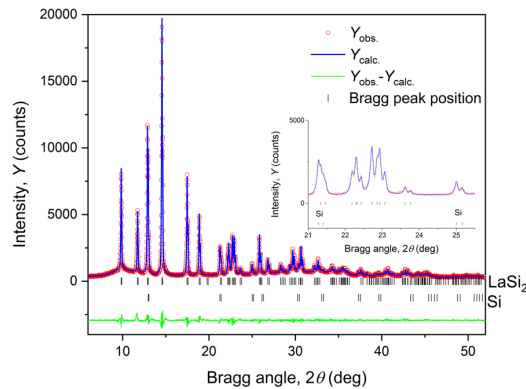


Fig. 2. X-ray powder diffraction pattern of the $\text{La}_{20}\text{Si}_{80}$ alloy containing LaSi_2 (79 wt.%) and Si (21 wt.%) crystalline phases. The inset highlights the area between 21 and 25.5 degree 2θ confirming presence of Si peaks.

Figures 3(a) and (b) are the resulting images that represent the topography and the near-field scattered amplitude maps of s_2 , respectively. Due to the spatially varying contents of LaSi_2 and Si, the near-field image displays a pronounced intricate pattern of islands and stripes of microstructures that is noticeably different from the topographic image of the same region. We next take a closer look by magnifying into a $10 \mu\text{m}$ by $10 \mu\text{m}$ region as shown in Fig. 4(a) that displays striking deep sub-micron features from the alloy. The corresponding AFM height scan is shown in Fig. 4(b) and presents a relatively flat surface within a variation of 30 nm. We further generated a correlation matrix, as shown in Fig. 4(c), which produced a Pearson correlation coefficient close to zero. Figure 5 and Fig. 6 shows a detailed analysis supporting the absence of the AFM and sSNOM crosstalk. Thus, our THz-sSNOM measurement on La–Si is capable of fully registering the conductivity contrasts stemming from the locally different electronic properties of the alloy.

The line cut in Fig. 4(d) as well as the whole $10 \mu\text{m}$ by $10 \mu\text{m}$ two dimensional scan exhibits a dichotomy between the higher tip-scattered amplitude of the metallic LaSi_2 and the lower tip-scattered amplitude of the insulating silicon. To identify any spectral features that can separate the two apparent phases of the alloy, we further demonstrate nanospectroscopy far below the diffraction limit with our THz light source spanning from 0.5 to 2 THz. Three positions in the

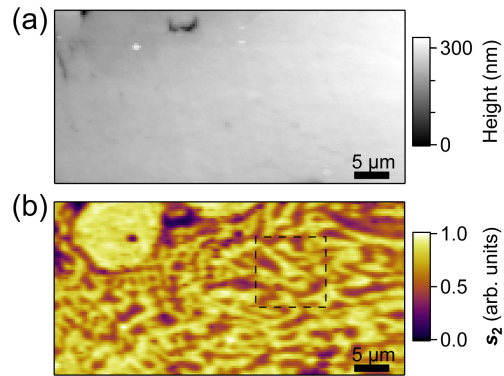


Fig. 3. (a) AFM topography map and (b) a simultaneously acquired spatial map of the THz near-field scattering amplitude s_2 measured on a representative region of La-Si.

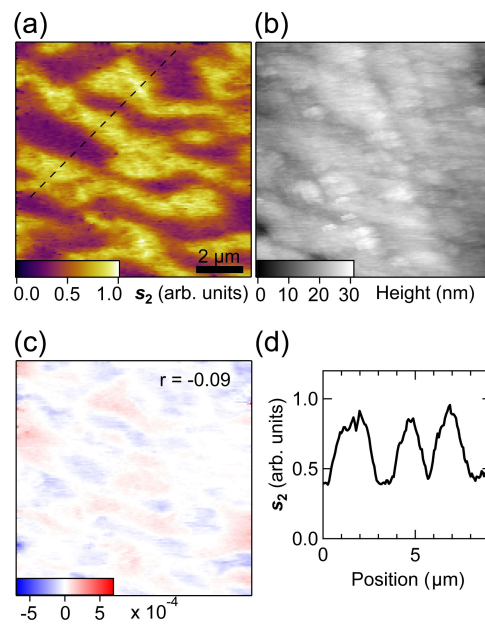


Fig. 4. (a) THz near-field scattering amplitude s_2 and (b) AFM height map of a region specified by the dashed box in Fig. 3(b). (c) The correlation matrix and correlation coefficient over the selected region. (d) Line profile taken along the dashed line in (a).

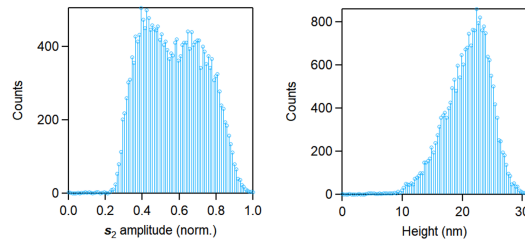


Fig. 5. THz s_2 distribution histogram (left) and height distribution histogram (right) from Fig. 4(a) and (b), respectively. We clearly see the bipartite distribution in the THz histogram corresponding to patches of different surface conductivity due to LaSi_2 and Si surface domains in the sample, while the topography is not significantly correlated with the THz s_2 signal and shows no such features.

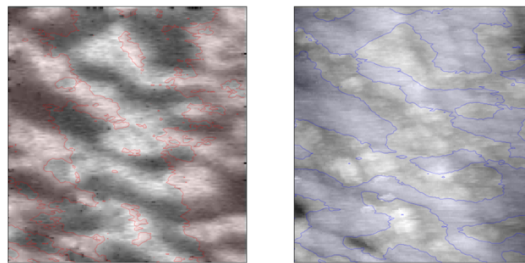


Fig. 6. THz near-field scattering amplitude s_2 map (left) and AFM topographical map (right) across the selected region of the La-Si sample identical to Fig. 4(a) and (b), respectively, but shown here in grayscale. The red (left) and blue (right) lines indicate the median contours for AFM height and THz s_2 amplitude, respectively, demonstrating that the two signals are not significantly correlated.

scanned area were selected to attain time-domain traces, which were then Fourier-transformed to obtain their respective amplitude spectra as shown in Fig. 7(a) and (b), respectively. One trace was taken at a bright region in the image scan, and another taken at a darker region. A third spectrum was acquired at another bright area to serve as a reference. Normalized to this reference spectrum, the outcomes of both the amplitude and phase spectra are plotted in Fig. 7(c) and (d). The relative amplitude shows a flat spectral response in the measured THz frequency range with the darker region yielding a signal that is only half of that from the relatively brighter regions which is consistent with what is exhibited in the time-domain traces and the line profile data. The s_2 THz signal essentially maps the local near-field THz susceptibility of the sample surface on a sub-100 nm length scale. Some outlying data points exist, e.g., most prominently around 1.1 and 1.7 THz, where there are dips in the near-field spectra. These occur presumably from a combination of interference effects in our backscattering setup geometry, tip-cantilever antenna resonances, and water absorption lines due to the lack of a purging system, as discussed in Refs. [18,19]. There is also an overall of approximately 0.2 radians or 11.5 degrees of phase difference between the two regions.

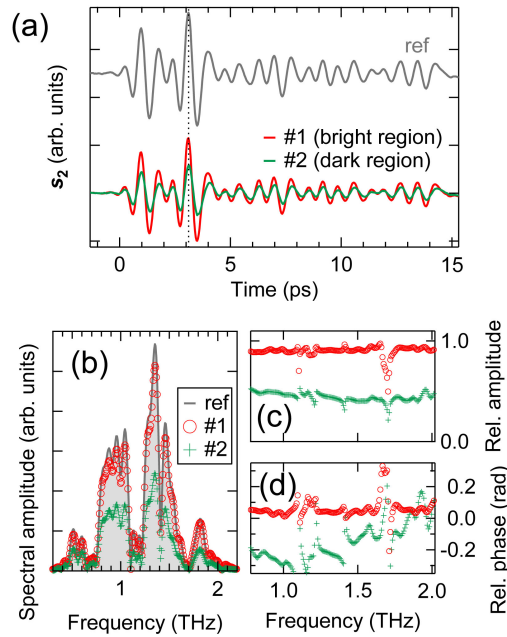


Fig. 7. (a) Measured THz near-field time traces at different locations of the sample. (b) Fourier-transformed spectra of the time traces in (a). A third spectrum was acquired at another bright region to serve as a reference in (a) and (b). (c) Relative amplitude spectra and (d) phase spectra with respect to the spectrum taken at the reference position.

3. Nano-compositional analysis of La-Si

For a quantitative analysis of the THz near-field amplitude image, the values of the scattering amplitude s_2 among pixels in the area of Fig. 4(a) are displayed in a histogram as shown in Fig. 8 (identically already shown in Fig. 5), which reveals two prevailing distributions that come from the bright metallic domain and the areas with the lower THz response. A gaussian fit to each of the distributions informs that the two peaks are located at a normalized s_2 value of 0.41 and 0.68. We estimate the scattered amplitude using a simplified point-dipole model and entering the dielectric values of 11.67 for silicon ($\epsilon_{\text{Si}} = 11.67$) and a practically imaginary value for LaSi_2 so that here the dielectric response is dominated by the metallic conductivity with the magnitude of the permittivity being in the order of $|\epsilon_{\text{LaSi}_2}| = 10^4$ [35]. This gives an s_2 amplitude ratio of 2.94 which is roughly around the ratio of the peak values of the fitted curves, i.e., $0.68/0.41 = 1.66$ (point-dipole model calculated for a p-polarized light at 1 THz frequency, 100 nm tapping amplitude, and 25 nm tip radius). A more accurate comparison with the experimental results could be performed through sophisticated numerical approaches but here we next focus on conducting a compositional analysis of the alloy phases. The phase difference is calculated to be ~ 0.1 radians which roughly matches with our measurement results in Fig. 7(d).

Furthermore, we can compare the area under the two fitted curves to estimate the average composition ratio of La-Si for this specific local region. This curve area ratio of 1.54 (Fit1 with width of 0.11833 and height of 435.22; Fit2 with width of 0.18511 and height of 428.41) indicates that the brighter LaSi_2 metallic domain is greater than the Si domain. We assume here that the depth of each of the microstructure domains extends beyond the decay distance of the scattered amplitude from the sample surface. To convert the volume ratio to weight, we use the theoretical density of 5 g/cm^3 for LaSi_2 and 2.33 g/cm^3 for Si. This leads to a weight ratio of $1.54 \times 5/2.33 = 3.30$ or 77 wt.% of LaSi_2 to 23 wt.% of Si. The value approaches close to

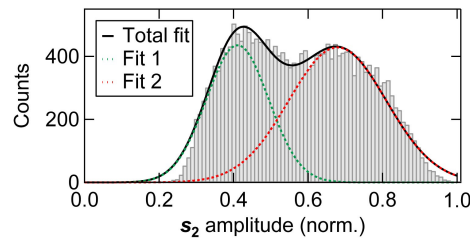


Fig. 8. Histogram of the THz near-field s_2 in image Fig. 4(a) and two overlapped gaussian fitted curves.

the expected ratio of 79/21 wt.% according to the stoichiometry. Therefore, we anticipate that THz-sSNOM to provide a compositional analysis of the microstructures down to the nanoscale.

4. Conclusion

We performed nano-compositional analysis at deep subwavelength dimensions in a rare-earth La–Si alloy using our THz-sSNOM setup. We expect that the distinct results from THz nano-imaging and nano-spectroscopy reported here can be extended to uncover unique low-frequency electrodynamics of detailed correlated electronic configurations. Therefore, our work paves the way to demonstrate the disentanglement and visualization of the local inhomogeneities of THz collective modes at nanometer length scales.

Funding. U.S. Department of Energy (DE-AC02-07CH11358, DE-AC02-07CH11359).

Acknowledgments. This work was supported by the Ames National Laboratory, the US Department of Energy, Office of Science, Basic Energy Sciences, Materials Science and Engineering Division under contract No. DE-AC02-07CH11358 (THz nanoscopy, synthesis and data analysis). Near-field model simulation and terahertz instrument development were supported by the U.S. Department of Energy, Office of Science, National Quantum Information Science Research Centers, Superconducting Quantum Materials and Systems Center (SQMS) under the contract No. DE-AC02-07CH11359.

Disclosures. The authors declare no conflicts of interest.

Data Availability. Data underlying the results presented in this paper are available from the corresponding author upon reasonable request.

References

1. B. Knoll and F. Keilmann, "Near-field probing of vibrational absorption for chemical microscopy," *Nature* **399**(6732), 134–137 (1999).
2. R. Hillenbrand, R. Taubner, and F. Keilmann, "Phonon-enhanced light–matter interaction at the nanometre scale," *Nature* **418**(6894), 159–162 (2002).
3. M. M. Qazilbash, M. Brehm, B.-G. Chae, *et al.*, "Mott transition in VO₂ revealed by infrared spectroscopy and nano-imaging," *Science* **318**(5857), 1750–1753 (2007).
4. J. Chen, M. Badioli, P. Alonso-González, *et al.*, "Optical nano-imaging of gate-tunable graphene plasmons," *Nature* **487**(7405), 77–81 (2012).
5. Z. Fei, A. S. Rodin, G. O. Andreev, *et al.*, "Gate-tuning of graphene plasmons revealed by infrared nano-imaging," *Nature* **487**(7405), 82–85 (2012).
6. F. Mooshammer, F. Sandner, M. A. Huber, *et al.*, "Nanoscale near-field tomography of surface states on (Bi_{0.5}Sb_{0.5})₂Te₃," *Nano Lett.* **18**(12), 7515–7523 (2018).
7. J. Nishida, A. H. Alfaifi, T. P. Gray, *et al.*, "Heterogeneous cation–lattice interaction and dynamics in triple-cation perovskites revealed by infrared vibrational nanoscopy," *ACS Energy Lett.* **5**(5), 1636–1643 (2020).
8. N. C. H. Hesp, I. Torre, D. Rodan-Legrain, *et al.*, "Observation of interband collective excitations in twisted bilayer graphene," *Nat. Phys.* **17**(10), 1162–1168 (2021).
9. H.-T. Chen, R. Kersting, and G. C. Cho, "Terahertz imaging with nanometer resolution," *Appl. Phys. Lett.* **83**(15), 3009–3011 (2003).
10. H.-G. von Ribbeck, M. Brehm, D. van der Weide, *et al.*, "Spectroscopic THz near-field microscope," *Opt. Express* **16**(5), 3430–3438 (2008).

11. J. Zhang, X. Chen, S. Mills, *et al.*, “Terahertz nanoimaging of graphene,” *ACS Photonics* **5**(7), 2645–2651 (2018).
12. H. T. Stinson, A. Sternbach, O. Najera, *et al.*, “Imaging the nanoscale phase separation in vanadium dioxide thin films at terahertz frequencies,” *Nat. Commun.* **9**(1), 3604 (2018).
13. N. A. Aghamiri, F. Huth, A. J. Huber, *et al.*, “Hyperspectral time-domain terahertz nano-imaging,” *Opt. Express* **27**(17), 24231–24242 (2019).
14. K. Moon, Y. Do, H. Park, *et al.*, “Computed terahertz near-field mapping of molecular resonances of lactose stereo-isomer impurities with sub-attomole sensitivity,” *Sci. Rep.* **9**(1), 16915 (2019).
15. A. Pizzuto, E. Castro-Camus, W. Wilson, *et al.*, “Nonlocal time-resolved terahertz spectroscopy in the near field,” *ACS Photonics* **8**(10), 2904–2911 (2021).
16. R. H. J. Kim, C. Huang, Y. Luan, *et al.*, “Terahertz nano-imaging of electronic strip heterogeneity in a Dirac semimetal,” *ACS Photonics* **8**(7), 1873–1880 (2021).
17. R. H. J. Kim, Z. Liu, C. Huang, *et al.*, “Terahertz nanoimaging of perovskite solar cell materials,” *ACS Photonics* **9**(11), 3550–3556 (2022).
18. R. H. J. Kim, J.-M. Park, S. J. Haeuser, *et al.*, “A sub-2 kelvin cryogenic magneto-terahertz scattering-type scanning near-field optical microscope (cm-THz-sSNOM),” *Rev. Sci. Instrum.* **94**(4), 043702 (2023).
19. R. H. J. Kim, J. M. Park, S. Haeuser, *et al.*, “Visualizing heterogeneous dipole fields by terahertz light coupling in individual nano-junctions,” *Commun. Phys.* **6**(1), 147 (2023).
20. S. Mastel, A. A. Govyadinov, T. V. A. G. de Oliveira, *et al.*, “Nanoscale-resolved chemical identification of thin organic films using infrared near-field spectroscopy and standard Fourier transform infrared references,” *Appl. Phys. Lett.* **106**(2), 023113 (2015).
21. L. Mester, A. A. Govyadinov, S. Chen, *et al.*, “Subsurface chemical nanoidentification by nano-FTIR spectroscopy,” *Nat. Commun.* **11**(1), 3359 (2020).
22. X. Yang, C. Vaswani, C. Sundahl, *et al.*, “Terahertz-light quantum tuning of a metastable emergent phase hidden by superconductivity,” *Nat. Mater.* **17**(7), 586–591 (2018).
23. X. Yang, C. Vaswani, C. Sundahl, *et al.*, “Lightwave-driven gapless superconductivity and forbidden quantum beats by terahertz symmetry breaking,” *Nat. Photonics* **13**(10), 707–713 (2019).
24. C. Vaswani, J. H. Kang, M. Mootz, *et al.*, “Light quantum control of persisting Higgs modes in iron-based superconductors,” *Nat. Commun.* **12**(1), 258 (2021).
25. L. Luo, D. Cheng, B. Song, *et al.*, “A light-induced phononic symmetry switch and giant dissipationless topological photocurrent in ZrTe₅,” *Nat. Mater.* **20**(3), 329–334 (2021).
26. L. Luo, M. Mootz, J. H. Kang, *et al.*, “Quantum coherence tomography of light-controlled superconductivity,” *Nat. Phys.* **19**, 201–209 (2022).
27. T. Li, L. Luo, M. Hupalo, *et al.*, “Femtosecond population inversion and stimulated emission of dense Dirac fermions in graphene,” *Phys. Rev. Lett.* **108**(16), 167401 (2012).
28. A. Patz, T. Li, X. Liu, *et al.*, “Ultrafast probes of nonequilibrium hole spin relaxation in the ferromagnetic semiconductor GaMnAs,” *Phys. Rev. B* **91**(15), 155108 (2015).
29. L. Luo, I. Chatzakis, A. Patz, *et al.*, “Ultrafast terahertz probes of interacting dark excitons in chirality-specific semiconducting single-walled carbon nanotubes,” *Phys. Rev. Lett.* **114**(10), 107402 (2015).
30. L. Luo, X. Yang, X. Liu, *et al.*, “Ultrafast manipulation of topologically enhanced surface transport driven by mid-infrared and terahertz pulses in Bi₂Se₃,” *Nat. Commun.* **10**(1), 607 (2019).
31. L. Luo, Z. Liu, X. Yang, *et al.*, “Anomalous variations of spectral linewidth in internal excitonic quantum transitions of ultrafast resonantly excited single-walled carbon nanotubes,” *Phys. Rev. Mater.* **3**(2), 026003 (2019).
32. X. Yang, L. Luo, C. Vaswani, *et al.*, “Light control of surface–bulk coupling by terahertz vibrational coherence in a topological insulator,” *npj Quantum Mater.* **5**(1), 13 (2020).
33. M. V. Bulanova, P. N. Zheltov, K. A. Meleshevich, *et al.*, “Lanthanum–silicon system,” *J. Alloys Compd.* **329**(1–2), 214–223 (2001).
34. J. Rodríguez-Carvajal, “Recent advances in magnetic structure determination by neutron powder diffraction,” *Phys. B* **192**(1–2), 55–69 (1993).
35. K. Abraha and D. R. Tilley, “Theory of far-infrared reflectivity and surface magnetic polaritons of rare-earth magnets,” *Infrared Phys. Technol.* **35**(5), 681–699 (1994).